Bioactive Materials 6 (2021) 1402–1412

Contents lists available at ScienceDirect

Bioactive Materials

journal homepage: www.sciencedirect.com/journal/bioactive-materials

Lightweight 3D bioprinting with point by point photocuring

Peng Zhang [a,c,1], Haoxuan Wang [b,c,1], Peng Wang [c], Yating Zheng [c], Linxiang Liu [d], Jun Hu [a], Yande Liu [a,***], Qing Gao [b,c,**], Yong He [b,c,*]

[a] School of Mechatronics & Vehicle Engineering, East China Jiaotong University, Nanchang, 330013, China
[b] State Key Laboratory of Fluid Power and Mechatronic Systems, School of Mechanical Engineering, Zhejiang University, Hangzhou 310027, China
[c] Engineering for Life Group (EFL), Suzhou, 215000, China
[d] Zhejiang University Hospital, Zhejiang University, Hangzhou, Zhejiang 310027, China

ARTICLE INFO

Keywords:
Three-dimensional (3D) bioprinting
Stereolithography bioprinting system
Compact
Low-cost
Tissue engineering
Cell printing

ABSTRACT

As photocrosslinkable materials, methacryloyl-modified hydrogels are widely used as bioinks in tissue engineering. Existing printing methods to use these hydrogels, including changing the viscosity of the material or mixing them with other printing components, have been explored, but their application has been limited due to low printing quality or high cost. In addition, the complex operation of bulky equipment restricts the application of these existing printing methods. This study presents a lightweight stereolithography-based three-dimensional (3D) bioprinting system with a smart mechanical and structural design. The developed bioprinter dimensions were 300 mm × 300 mm × 200 mm and it can be placed on a benchtop. The equipment has a mini bioink chamber to store a small amount of bioink for each printing. We systematically investigated the point-by-point curing process in the 3D bioprinting method, which can print mixed cells accurately and have good biocompatibility. Here, we provide a compact, low-cost stereolithography bioprinting system with excellent biocompatibility for 3D bioprinting with methacryloyl-modified hydrogels. It can be potentially used for drug screening, studying pathological mechanisms, and constructing biological disease models.

1. Introduction

Three-dimensional (3D) bioprinting is a technique that combines biological culture and additive manufacturing and has shown great potential in tissue engineering and regeneration medicine [1–5]. With the aim of achieving a breakthrough in the functional application of 3D bioprinting, the research direction in this field has gradually shifted from shape to function [6–8]. Selecting the appropriate bioink is key to achieve the challenging goal of functional bioprinting. Recently, natural hydrogels modified with methacryloyl (e.g., GelMA, Hyaluronic Acid Methacryloyl (HAMA), Silk fibroin Glycidyl Methacrylate (Sil-MA), *etc.*) have been widely used as bioink. While retaining the biocompatibility of natural hydrogels, modified hydrogels easily crosslink upon light exposure due to the presence of photocrosslinkable methacrylamide groups [9–11]. However, these hydrogels still have inherent flaws, including low viscosity and slow crosslinking, which lead to poor printability and limit printing [12]. Therefore, it is necessary to develop an efficient method combined with a compact and low-cost device for the printing of photocrosslinkable bioinks.

Photocrosslinkable hydrogels are currently used as bioinks in various bioprinting techniques, including inkjet-based, laser-assisted, and extrusion-based bioprinting [13–16], as well as other printing methods [17–22]. In inkjet-based bioprinting, photocrosslinkable hydrogels are first converted into microdroplets, which are then received using a droplet receiver and subsequently photocrosslinked with visible light [23], which has the advantages of low cost, high cell viability and high speed. However, this technique has proven to be difficult for large-scale manufacturing of 3D structures using photocrosslinkable hydrogels due to its small driving pressure and low printing accuracy. Extrusion-based bioprinting is the most widely used printing technique due to its

* Corresponding author. State Key Laboratory of Fluid Power and Mechatronic Systems, School of Mechanical Engineering, Zhejiang University, Hangzhou 310027, China.
** Corresponding author. State Key Laboratory of Fluid Power and Mechatronic Systems, School of Mechanical Engineering, Zhejiang University, Hangzhou 310027, China.
*** Corresponding author. School of Mechatronics & Vehicle Engineering, East China Jiaotong University, Nanchang, 330013, China.
E-mail addresses: liuyande@ecjtu.jx.cn, jxliuyd@163.com (Y. Liu), gaoqingvc@zju.edu.cn (Q. Gao), yongqin@zju.edu.cn (Y. He).
[1] These authors contributed equally to the work).

https://doi.org/10.1016/j.bioactmat.2020.10.023
Received 3 August 2020; Received in revised form 27 September 2020; Accepted 27 October 2020
2452-199X/© 2020 The Authors. Production and hosting by Elsevier B.V. on behalf of KeAi Communications Co., Ltd. This is an open access article under the CC BY-NC-ND license (http://creativecommons.org/licenses/by-nc-nd/4.0/).

simplicity, relatively low cost, and compatibility with various materials. As a result, many extrusion-based strategies for printing with photocrosslinkable bioinks have been developed, including pre-crosslinking to increase the viscosity of the bioink [24], post-crosslinking to quickly cure the photocrosslinkable hydrogel [25], in situ crosslinking to retain the stability of the filament [26], and two-step crosslinking to improve the printability of the ink mixture [27]. Extrusion-based bioprinting has been widely studied and used in various applications, including sustained drug release, angiogenesis, and cartilage differentiation. The aforementioned methods can successfully print photocrosslinkable bioink, but in most of them bioink preparation involves altering the viscosity of the material or mixing it with other printable components [27]. Such as mixing it with alginate to increase the strength of the hydrogel [28] or mixing it with nanoclay to increase the viscosity of the hydrogel [29], which can enhance its supporting performance. However, with the increase of the strength and viscosity of the hydrogel, the cell damage due to shear stress will increase during the printing process and lead to reduced cell viability; also, photocrosslinking is only used for final shaping [24,29,30]. In addition, extrusion-based bioprinting uses a nozzle, which also produces shear stress, resulting in reduced cell viability and poor printing accuracy [31]. At present, the research on the accuracy of bioprinting usually focuses on the accuracy analysis of the hydrogel filament obtained from extrusion printing, including the evaluation of filament collapse and filament fusion of hydrogel [32], the evaluation of the extrusion state of the filament [33], the evaluation of the standard grid structure of filament printing [34], and the analysis of the relationship between material composition and printing accuracy [35]. However, currently, most of the bioprinting systems are extrusion-based, and there is no report on the systematic analysis of stereolithography (SL) bioprinting methods. Therefore, to achieve the high precision and biocompatibility required in scientific research, a manufacturing method based on the principle of visible light curing needs to be urgently developed.

SL is a rapid prototyping technique that uses a visible laser beam to solidify photocrosslinkable materials *by* a point-by-point curing technique to construct complex 3D prototypes with high fidelity. This technique allows the manufacture of microscale bionic structures [36,37]. Besides, SL is a nozzle-free method, which results in high cell viability exceeding 95% and print repeat accuracy reaching 10 μm [38]. Consequently, SL has great advantages in biocompatibility and manufacturing accuracy [39]. However, most commercial SL equipment can only print photosensitive resin, which is not suitable for printing soft photocrosslinkable hydrogels [40–42]. Only a few SL devices can print photocrosslinkable hydrogels [43,44]. In addition, high cost and the inconvenience involved in the aseptic operation of bulky equipment limit the application of SL in biological manufacturing research. SL printing of photocrosslinkable hydrogels has been used in previous studies, but the printed structures in such studies showed no vertical change in shape, which is not strictly 3D printing [45]. Accordingly, a SL bioprinting system consisting of efficient printing crafts and a compact, low-cost device with superior biocompatibility has been developed.

In this study, we propose a lightweight SL bioprinting system that is compact, easy to operate, cost-effective, and with high cell viability. A low-cost SL device, equipped with a visible laser transmitter and a Petri dish, was first shown to rapidly print GelMA hydrogel. With this device, the printing light source is devised by replacing the commercial laser projector with a visible laser transmitter, thus reducing the cost price to USD758.537 (September 2019) and consuming a considerably small amount of bioink for each printing (in the milliliter scale). Furthermore, to establish a SL bioprinting system to solve the problems of the poor printability and long crosslinking time of photocrosslinkable hydrogels, we focused on studying the point-by-point curing-based 3D bioprinting method in order to accurately construct complex structures. In this study, GelMA hydrogel is regarded as a representative light-curable hydrogel for printability research due to its wide range of applications and superior biological properties. In summary, this study systematically investigated the point-by-point curing process in the 3D bioprinting method, evaluated the printing results by establishing characteristic values, and verified its biocompatibility. This study can be used as a reference for drug screening, as well as for the study of the pathological mechanism and construction of biological disease models.

2. Materials and methods

2.1. Preparation of materials

In this study, 5, 10, and 15% (w/v) solutions of photocrosslinkable hydrogels were prepared by dissolving methacryloyl gelatin (GelMA, EFL-GM-90; Suzhou Yongqinquan Intelligent Equipment Co., Ltd., Suzhou, China) in Minimum Essential Medium (MEM) containing 0.4%–0.6% (w/v) of the photoinitiator lithium phenyl-2,4,6-trimethylbenzoylphosphinate (LAP; Suzhou Yongqinquan Intelligent Equipment Co., Ltd.) and 0.2%–0.3% (w/v) of New Coccine (Light Blocker B113325; Aladdin Industrial Corporation, Shanghai, China) with continuous stirring at 37 °C for 1 h.

2.2. Setup of the stereolithography bioprinting system

The SL bioprinting system needs to perform the 3D movement of the platform, generate a visible laser, and have temperature control. The final dimensions of the 3D motion platform of the device are 300 mm (L) × 300 mm (W) × 200 mm (H) with a 10-μm printing repeatability, and a printable area of 20 mm (L) × 20 mm (W) × 30 mm (H). The visible laser emitter acting as a curing light source is connected to the computer and placed directly above the printing groove to irradiate the visible laser spot into the GelMA ink. The visible laser emits light at 405 nm wavelength, and the laser spot diameter is 1 mm. The light source has an input power of 200 mW and a working voltage of 3.3 V. A temperature control platform is attached below the printer trough to prevent the GelMA hydrogel from condensing at room temperature. The temperature of the platform is controlled with an ATmega328 P microcontroller (Microchip Technology Inc., Chandler, AZ, USA), which is heated by a 12 V-rated voltage heating film with a heating area of 40 mm (L) × 40 mm (W) and rated heating power of 24 W.

2.3. Rheological characterization of the bioinks

In the rheological characterization of bioinks, 5 and 10% GelMA hydrogels were evaluated. First, the hydrogels were scanned at the printing temperature, the clamp diameter was set to a 40 mm parallel plate, the fixed strain was 1%, the angular frequency was 5 rads, and the time scanning was performed at 37 °C. Second, the scanning time of the photocuring process of the hydrogel was performed. The diameter of the fixture was set as the 40 mm parallel plate, with a fixed strain of 1%, and an angular frequency of 2 rad/s, and was kept at 37 °C. The 405-nm visible photochemical crosslinking was performed at 30 s and the illumination time was 20s.

2.4. Printability analysis of the GelMA ink

In this study, a SL bioprinting system was used to print GelMA hydrogel spots. The GelMA ink solutions consisted of GelMA (5, 10, and 15%) solutions with LAP (0.25%) and New Coccine (0.25%). The printing process is performed at 37 °C. The cross-section of the "curing spot" was observed using a stereomicroscope, and the visible light-curing spot height and visible light-curing spot width were determined. By controlling the GelMA concentration and printing speed, the relationship between these parameters and *cylindricity* was determined. Subsequently, to systematically evaluate the degree of linking between points, we printed 2 adjacent GelMA hydrogel spots and measured the cross-section. By controlling the printing speed, GelMA concentration, and interval, the relationship between these parameters and the *Overlap Ratio* was determined.

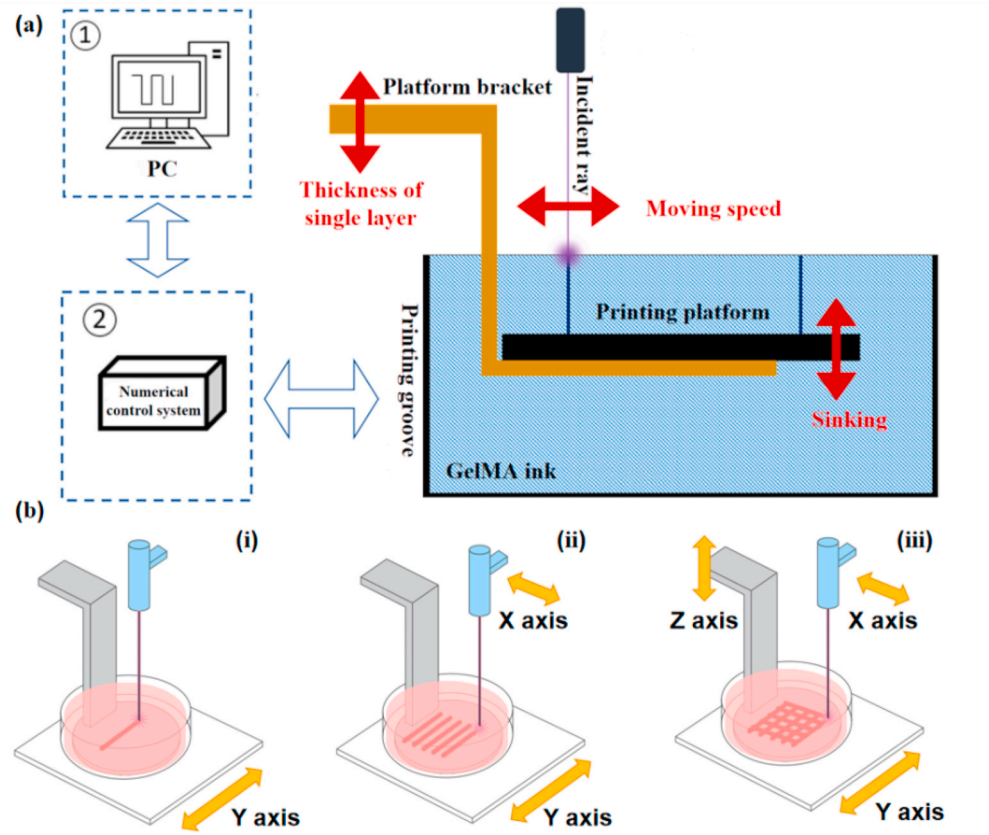

Fig. 1. Design of the stereolithography bioprinting system. (a) Diagram of the stereolithography bioprinting system. The photocrosslinkable hydrogel structure is formed by controlling the motion of the visible laser emitter and the printing platform; (b) Fabrication of the stereolithography bioprinting system: (i) line forming, (ii) surface forming, and (iii) 3D structure forming.

2.5. Mechanical characterization of the constructs

In the mechanical test, two kinds of grid scaffolds with GelMA concentration of 5 and 10% were prepared. The overall dimensions of the grid stent were 10 mm × 10 mm × 5 mm. The grid stent contained 16 square through holes with side length of 1 mm, and the calculated cross-sectional area was 84 cm^2. In the stress-strain test, the slope of the first 10% strain section of the stress-strain curve is taken as the Young's modulus of the hydrogel grid structure.

2.6. Biocompatibility characterization

2.6.1. Cell culture and fabrication of crosslinkable bioink

Unless otherwise stated, mouse bone marrow mesenchymal stem cells (mBMSCs) were cultured in Dulbecco's modified Eagle's medium (DMEM) supplemented with streptomyces (100 μg/mL), 10% fetal bovine serum, and 1% penicillin (100 units/mL). The mBMSCs were cultured in 75 cm^2 cell culture flasks incubated at 37 °C in 5% CO_2, and the culture medium was replaced every 2 d. When the cell confluence reached 90%, the mBMSCs were passed after washing with phosphate-buffered saline (PBS) and detachment using the trypsin-ethylenediamine tetraacetic acid (trypsin-EDTA) separation method (0.25% trypsin-EDTA and incubation in the incubator at 37 °C in 5% CO_2 for 3 min). Subsequently, the cell suspension was centrifuged for 5 min at 1,000 rpm, supernatant was removed, and the cells were resuspended in MEM medium at a final cell concentration of 2×10^6 cells/mL. The photocrosslinkable bioink was prepared by mixing mBMSCs into the GelMA hydrogel. After reducing the concentration of the light blocking agent (New Coccine) in order to reduce its damage on the cells, a sterile hydrogel consisting of 5% GelMA, 0.4% LAP, and 0.2% New Coccine was obtained. Ultimately, the photocrosslinkable hydrogel was mixed with the cells in a volume ratio of 1:1, the final concentration of GelMA in the bioink was 5% (w/w), and the cell density was 1×10^6 cells/mL.

2.6.2. Cell viability analysis

Cell viability was analyzed using the LIVE/DEAD Viability/Cytotoxicity Kit (KeyGen Biotechnology Co., Ltd., Nanjing, China). Cell-laden scaffolds were first rinsed 3 times with PBS. A PBS solution containing 8 μM propidium iodide (PI) and 2 μM calcein AM was added to the cell-laden scaffolds, which were then incubated in the dark for 20–35 min and washed 3 times with PBS. The cell-laden scaffolds were eventually observed and imaged under an Olympus FV-3000 confocal laser scanning fluorescence microscope (Olympus Corporation, Tokyo, J). The sample of the scaffold to be tested was placed under the confocal laser scanning microscope for 5 d, and images showing the survival of cells were captured on days 1, 3, and 5. The calculation formula is given by

$$\frac{N_l}{N_t} \times 100\%$$

where N_l is the number of living cells, and N_t is the total number of cells.

2.6.3. Cell morphological analysis

F-actin and nuclei were stained with phalloidin-tetramethylrhodamine B isothiocyanate (phalloidin-TRITC; YEASEN BioTech Co., Ltd., Shanghai, China) and 4′,6-diamidino-2-phenylindole (DAPI; Solarbio, Beijing, China), respectively, to characterize the cytoskeleton and assess cell morphological changes. After washing cell-laden scaffolds 3 times in PBS and fixing in 4% paraformaldehyde for 30 min, they were washed with PBS and infiltrated with 0.5% Triton X-100 for 5 min. Afterwards, the cell-laden scaffolds were washed 3 times with PBS

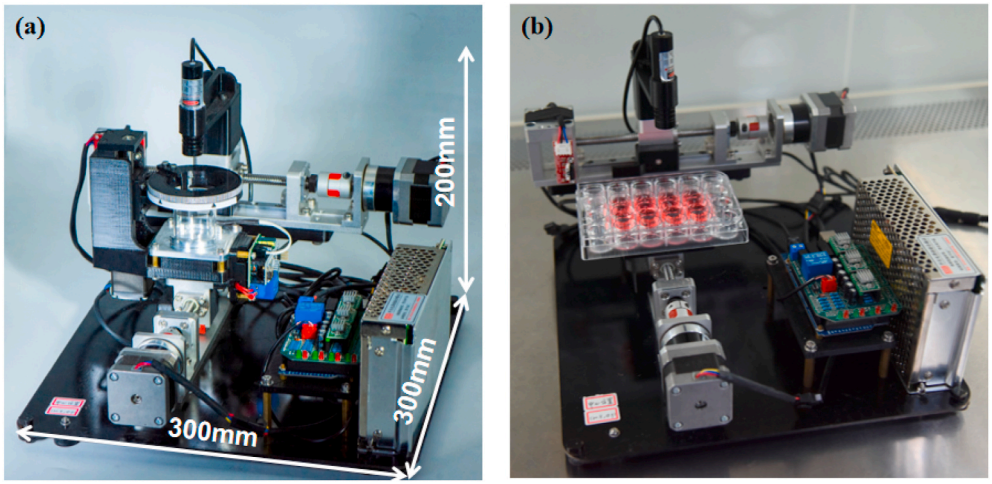

Fig. 2. Stereolithography bioprinting device. (a) Overall appearance of device and (b) The stereolithography bioprinting device placed on an ultraclean worktable (the material trough is replaced with a 24-hole plate).

Table 1
Cost of the proposed system.

Item	Amount	Cost (USD)
Linear Module (X axis、Y axis)	2	506.16
Linear Module (Z axis)	1	70.3
visible laser transmitter	1	40.774
Circuit controller	1	14.06
Power Supply	1	7.733
Heating Film	1	2.812
Fuselage Metal Frame	1	28.12
PLA Parts	500 g	4.218
Total		758.537

and stained with phalloidin-TRITC (0.1 μM) in the dark for 30 min. The cell-laden scaffolds were washed again with PBS and stained with DAPI (10 μg/mL) for 10 min, and ultimately washed with PBS. Images were eventually captured under the confocal laser scanning fluorescence microscope.

3. Results and discussions

3.1. Stereolithography bioprinting system design

A schematic representation of the printing of a photocrosslinkable bioink for use in a SL bioprinting system is shown in Fig. 1(a). Due to its photocrosslinkable characteristic, the bioink was easily photocrosslinked with visible light and transformed into a gel. The curing process of the ink using a visible laser emitter to form a hydrogel point and the fabrication of the pattern point-by-point by stacking the hydrogel point are shown in Fig. 1 (b).

The adhesion ability between printed layers and the supporting performance of the bioink are highly desired during printing to ensure that the bioinks meet the requirements of SL bioprinting, namely, the fluidity of the bioink. As shown in Fig. S1, the bioink exhibits excellent adhesion, and the fluidity of the bioink supports the automatic replenishment of printing materials. Moreover, the self-supporting property of the bioink enables the construction of complex structures. The suitability of the photocrosslinkable hydrogel for its application in a SL bioprinting system is established by its characteristics.

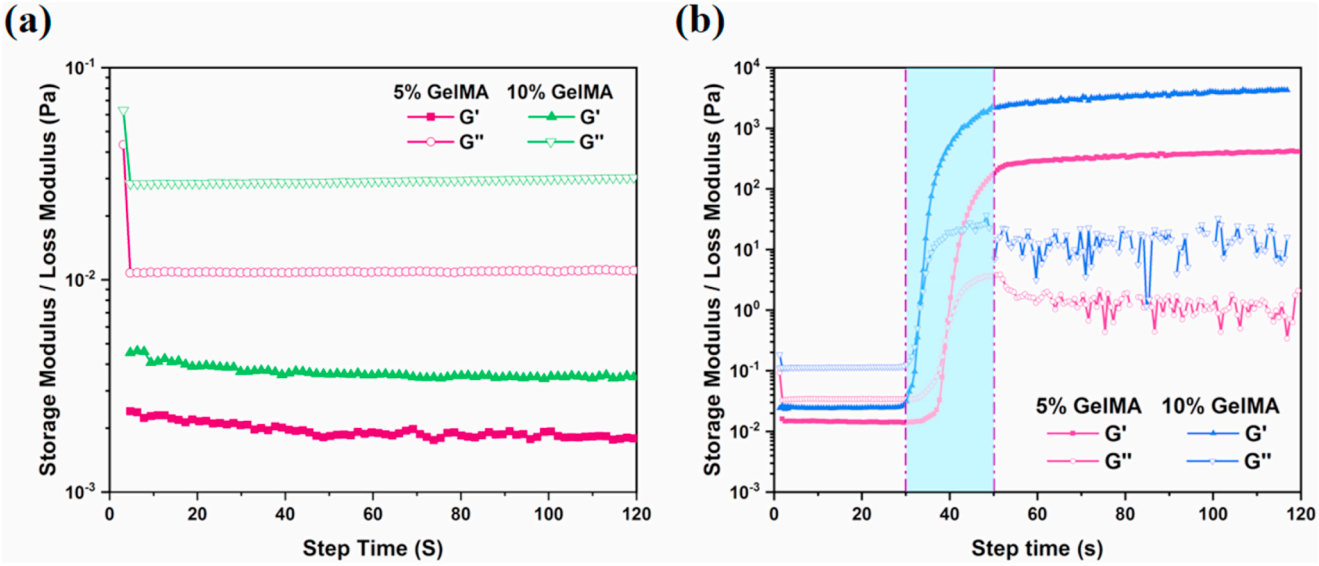

Fig. 3. Rheological characterization of the bioinks. (a) The time scanning test at the printing temperature; (b) The time scanning test of the visible light-curing process.

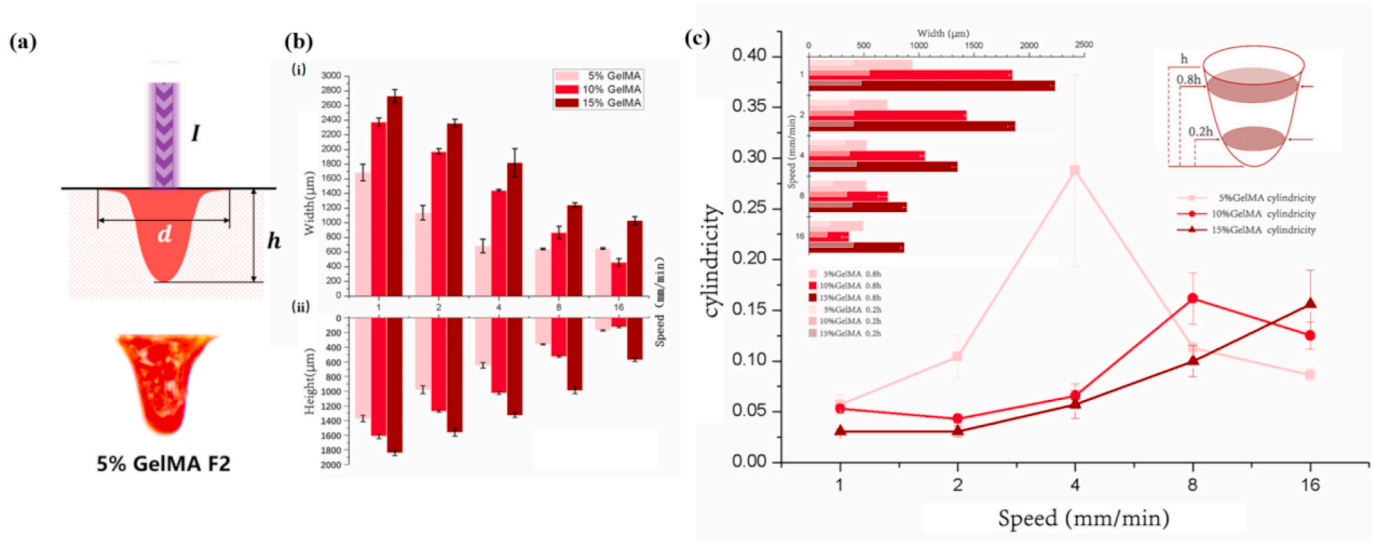

Fig. 4. Analysis of the printability of photocrosslinkable hydrogel during spot clearing curing. (a) The schematic and actual effect of visible light-curing spot height (*h*) and visible light-curing spot width (*d*); (b) Effect of printing speed on the (i) visible light-curing spot width and (ii) visible light-curing spot height; (c) Effects of printing speed and GelMA concentrations on *cylindricity*.

3.2. Setup of the stereolithography bioprinting system

To meet the printing accuracy requirement for the photocrosslinkable hydrogel, the device needs to have high repeated positional accuracy, compact structure, and superior biocompatibility. To achieve these goals, we set the SL bioprinting device, which consisted mainly of three linear modules and a visible laser emitter (see Fig. 2). We used a Petri dish or a 24-well plate as the printing groove. The amount of ink needed for each printing was only a few milliliters. The generally compact structure (300 mm × 300 mm × 200 mm) of the device was suitable for operating on an ultraclean table. The repeated positioning accuracy of the three-axis motion of this device can reach 50 μm. Regarding costs, the proposed SL bioprinting device costs considerably less, compared with existing bioprinting equipment (Table S3, Table S4), and the final cost can be kept to about USD758.537 (Table 1). Therefore, the parameters of the proposed SL bioprinting device met the requirements for printing photocrosslinkable hydrogels and the device is suitable for research on 3D bioprinting with hydrogel.

3.3. Analysis of the printability of the photocrosslinkable hydrogel

The rheological properties of the material determine its suitability for printing and thus can reveal whether the hydrogel meets the printing requirements. Accordingly, we verify the changes in the printing process by evaluating the rheological properties of the 5 and 10% GelMA hydrogel solutions used for printing, in order to verify that the bioink meets the requirements for SL-based 3D bioprinting.

The two different concentration solutions of GelMA hydrogels used for printing were scanned at the printing temperature (Fig. 3(a)) and the visible light-curing process (Fig. 3(b)). The time scanning test results at the printing temperature reveal that the loss modulus (G″) of the two different concentration solutions of GelMA hydrogel remains at a stable value at 37 °C. Additionally, the G″ is much larger than the storage modulus (G′), indicating that the state of the GelMA hydrogel is liquid, and the loss modulus of the 10% GelMA hydrogel solution is clearly stronger than that of the 5% GelMA hydrogel solution. On the other hand, at 37 °C, the strength of the 10% GelMA hydrogel solution is stronger than that of the 5% GelMA hydrogel solution, and also has better molding accuracy. The time scanning test results of the visible light-curing process reveal that after applying blue light for 20 s to two kinds of printing solutions at 37 °C, at first, the modulus changes of the two solutions show that the G″ is much larger than the G'. Then, the G′ of the GelMA hydrogel solution increases gradually with the increase of illumination time, and eventually the value of the G′ exceeds the value of the G″. After stopping the illumination, the G′ of GelMA hydrogel remained stable, and the G′ of the 10% GelMA hydrogel was much higher than that of the 5% GelMA hydrogel. These findings show that during the printing process, the GelMA hydrogel gradually changes from a flowable liquid to a photocrosslinked and solidified gel and maintains a stable strength after visible light-curing. The strength of the higher concentration GelMA hydrogel is significantly stronger than that of lower concentration GelMA hydrogel, which is beneficial to printing. Through the analysis of the rheological test results, we can determine whether the strength and curing time of the GelMA hydrogel are suitable for SL bioprinting.

The printing performance of the GelMA hydrogel needs to be evaluated to determine the optimal printing parameters to use the SL bioprinting system for printing high-precision photocrosslinked hydrogel structures. The process of printing the photocrosslinkable hydrogel is divided into two steps: (i) curing the ink to form hydrogel spots and (ii) connecting the hydrogel spots to form a 3D structure. Therefore, printability analysis must be conducted at these two steps.

3.3.1. Analysis of the printability of the photocrosslinkable hydrogel during spot curing

During spot curing, the printings with the two different concentration solutions of photocrosslinkable hydrogel exhibit a "normal distribution" pattern (Fig. 4(a)) with two characteristics: (i) Due to light scattering and the excitation of photocrosslinkable methacrylamide groups in the hydrogels, the GelMA ink around the printing pattern is solidified, and the lateral dimension of the cured hydrogels is larger than the diameter of the visible laser spot. (ii) The width of the cured hydrogel decreases with the increase of the depth of the cured hydrogel. The visible light-curing spot height and width are affected by the hydrogel concentration and printing speed, as shown in Fig. 4(b). At the same GelMA hydrogel concentration, the curing width and depth are inversely proportional to the printing speed: as the printing speed increases, both the curing height and width decrease. At the same printing speed, the depth of the curing light and width of the curing area are proportional to the concentration of the GelMA solution.

In this study, *cylindricity* describes the accuracy of the printed spot ($cylindricity = R(0.2h)^2/R(0.8h)^2$, where h is the height of the hydrogel).

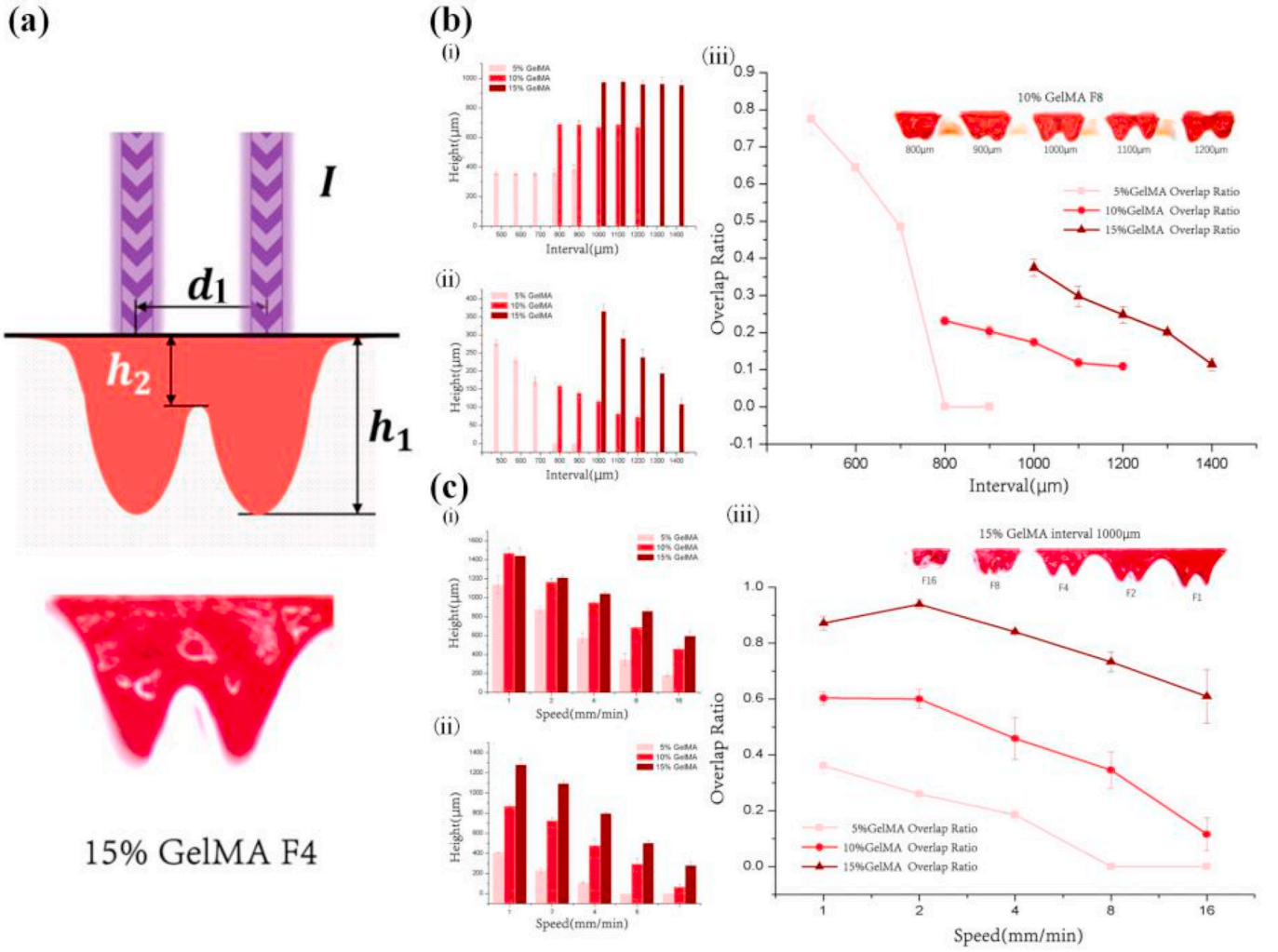

Fig. 5. Analysis of the printability of the photocrosslinkable hydrogel during cured-spot linking. (a) Schematic and comparison of intervals (d_1); (b) Effects of the interval on (i) h_1 and (ii) h_2 and (iii) the *overlap ratio*; and (c) Effect of speed on (i) h_1, (ii) h_2, and (iii) *overlap ratio*.

The *cylindricity* ranges from 0 to 1; the closer it is to 1, the higher the accuracy of the cured hydrogel spot; the closer it is to 0, the lower the accuracy of the cured hydrogel spot. The results in Fig. 4(c) show that the *cylindricity* value increases with increasing printing speed and decreases when it reaches the peak, whereas it decreases with increasing GelMA concentration. The visible light-curing spot width of the three hydrogels is inversely proportional to the printing speed and directly proportional to the GelMA concentration. The line chart shows that the hydrogel does not exhibit a monotonically increasing *cylindricity* similar to that of the visible light-curing spot width and height, but shows a peak (5% GelMA: 4 mm/min, 10% GelMA: 8 mm/min, 15% GelMA: 16 mm/min). The *cylindricity* of the hydrogel prepared at the peak printing speed is higher, and too low or too high printing speeds prevents printing of a suitable hydrogel structure. Different GelMA concentrations correspond to different *cylindricity* peak positions. Thus, we can obtain the optimal *cylindricity* by changing the printing parameters. Experimental data indicate that as the concentration of GelMA hydrogel increases, the printing speed of the peak *cylindricity* also increases, and the position of the peak moves in accordance with the GelMA hydrogel concentration.

3.3.2. *Analysis of the printability of the photocrosslinkable hydrogel during linking of cured spots*

During the linking of cured spots, the link relationship between points determines the formation of the surface and 3D hydrogel structure of the 3D hydrogel (Fig. 5(a)). The degree of linking between two cured spots is affected by the concentration of the photocrosslinkable hydrogel, interval, and printing speed (Figs. 5(b) and 4(c)). The *Overlap Ratio* describes the linking degree of adjacent cured hydrogel spots (*Overlap Ratio* $= h_2/h_1$, where h_1 is the average cure depth of two adjacent hydrogel spots, and h_2 is the cure depth at the overlap of two adjacent hydrogel spots). The *Overlap Ratio* ranges from 0 to 1, and the closer it is to 1, the higher the degree of linking between two cured GelMA spots, and vice versa. The results shown in Fig. 5(b)(i) and 4(b) (ii) reveal that h_1 increases with increasing GelMA concentration. However, at the same GelMA concentration, h_1 does not change with increasing interval, whereas h_2 decreases with increasing interval. Also, the results in Fig. 5(b)(iii) show that the *Overlap Ratio* value decreases with increasing interval. Due to differences in the curing width at different GelMA concentrations, the *Overlap Ratio* test interval segments vary. For example, when the interval is 1000 μm, the *Overlap Ratio* of the 15% GelMA hydrogel with a larger curing width can reach 15%, but the 5% GelMA hydrogel with a smaller curing width results in complete detachment. Notably, due to the sparse microstructure and poor mechanical properties of the low-concentration GelMA hydrogel, its spot tends to adhere. The tension it produces in the solution leads to the large *Overlap Ratio* fluctuations of the 5% GelMA hydrogel, which can only qualitatively show the *Overlap Ratio* trend. In addition, higher GelMA hydrogel concentrations can achieve a higher *Overlap Ratio* as the interval decreases. The results in Fig. 5(c)(i) and 4(c)(ii) reveal that h_1 and h_2 decrease with increasing printing speed. The results in Fig. 5(c)(iii)

Table 2
GelMA printing window.

Printing parameters	Printing window
GelMA concentration	5% ~ 15%
Printing speed	2 mm/min ~ 40 mm/min
Layer thickness	50 μm ~ 200 μm
Photoinitiator (LAP) concentration	0.4% ~ 0.6%
Light absorbent (New Coccine) concentration	0.2% ~ 0.3%

also show that the *Overlap Ratio* decreases with increasing printing speed. The *Overlap Ratio* curves depicting different GelMA concentrations show that the *Overlap Ratio* increases in a gradient after curing with GelMA solutions at different concentrations.

In summary, after systematically evaluating the point-by-point curing 3D bioprinting method, the linear relationship between various parameters, including GelMA concentration, printing speed, and layer thickness, was determined. When the GelMA concentration was less than 5%, the strength of the cured GelMA spots was considerably low, and printing could not be controlled. On the other hand, when the GelMA concentration exceeded 15%, the curing speed was considerably high, rendering the printing window of other parameters too small (also known as "nonprintable parameters"). After the experimental evaluation, the printing window of the main parameters related to SL bioprinting was determined (Table 2).

3.3.3. Printing of complex 3D structures

During the formation of the 3D structure using the SL bioprinting system, the printing window further decreased with a change in the print structure. In this study, we further investigated the effect of the selection of the printing parameters of specific 3D structures on two levels complex geometric structures and bionic tissue structures to verify the printability of photocrosslinkable hydrogels and determine the optimal printing parameters. The resulting printing parameters are listed in Table S1.

Based on the aforementioned printability analysis, the optimal printing parameters were selected to manufacture the complex geometric structure, such as the grid structures, the text "EFL", and a large-inclination structure (Fig. 6). The grid structure was the simplest and easiest to 3D structure (Fig. 6(a)(i)) to construct with photocrosslinkable hydrogels 3D bioprinting. Numerous 3D bioprinting models are currently based on the grid structure, and the hydrogel structure with an appropriate mesh size contributes to cell growth. Various grid structures printed using the SL bioprinting system mainly vary in the grid line spacing (Fig. 6(a)(ii)). With an increase in the porosity of the grid structure, the grid structure exhibits increased resistance to deformation. Besides, the SL bioprinting system can print thin-walled structures and large-inclination structures (Fig. 5(b) and (c)) that are difficult to print with conventional printers.

A complex geometric structure is an important feature in bionic structure printing (Fig. 7), and the bionic structure manufactured in this study has the aforementioned complex geometric structure. The porous scaffold (Fig. 7(a)) and thin-plate liver unit structure (Fig. 7(b)) are a combination of a grid structure and a thin-walled structure. Meanwhile, the truss liver unit structure (Fig. 7(c)) is a combination of a grid structure and a large-inclination structure. The functionalization of hydrogels can be achieved by constructing its biomimetic structure. In summary, by combining the selected optimal parameters in the printing process, we can construct a complex geometric model, which is difficult to manufacture using traditional 3D bioprinting. Subsequently, the bionic structure can be printed to simulate the complex geometric shape of biological tissues.

3.4. Mechanical characterization of the constructs

In order to perform the mechanical characterization of the constructs, a compression test of the printed grid structure was carried out (Fig. 8). The compression test revealed that the stress and Young's modulus of the printed structure increased with the increase of the hydrogel concentration (Fig. 8A and Fig. 8B) (9.432 ± 0.276 and 25.587 ± 0.562 KPa, respectively). There is a significant difference in Young's modulus between the high concentration grid structure and low concentration grid structure. These results show that the concentration of the hydrogel improves the mechanical strength of the printing structure.

3.5. Biocompatibility characterization

To determine the influence of the SL bioprinting system on biocompatibility, we printed mBMSC-laden GelMA scaffolds (Table S2) and subsequently cultured the mBMSCs on the scaffold. Considering the effect of the intensity of the visible light-curing of the GelMA on cell viability, we chose the 5% GelMA for cell printing.

3.5.1. Cell viability analysis

Images of cells cultured in the GelMA scaffolds for 5 days are shown in Fig. 9. The analysis of cell viability by staining the mBMSCs-laden GelMA scaffolds using the LIVE/DEAD kit, shown in Fig. 9 (a), revealed that the cell survival rate in GelMA scaffolds printed by the SL bioprinting system is considerably high, exceeding 95%, and the cell distribution is concentrated on the surface of GelMA scaffolds. In addition, as shown in Fig. 9(b) and (d), the cells are uniformly dispersed on

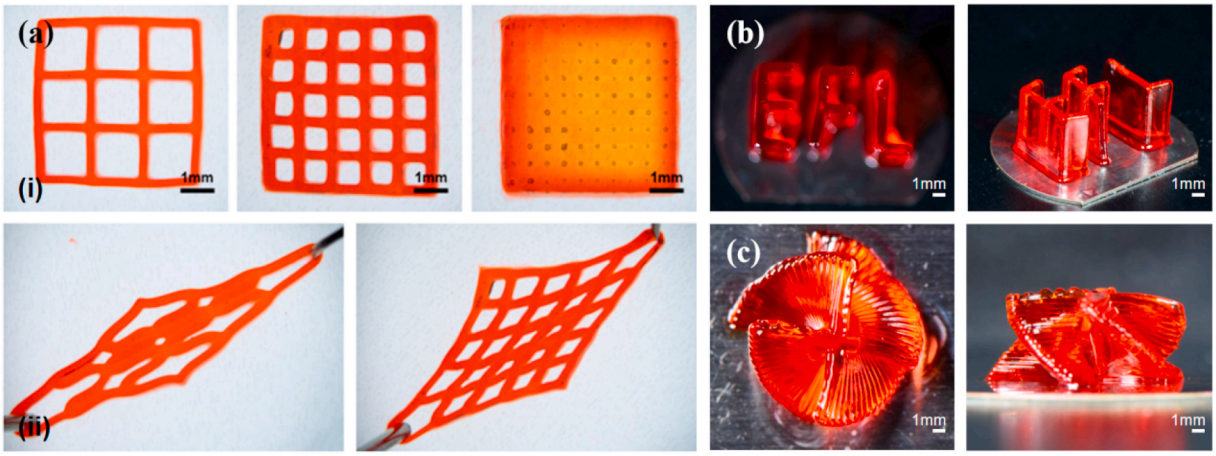

Fig. 6. Printed complex geometric structures. (a) Printed grid structures with different (i) porosity levels and (ii) degrees of tensile deformation; (b) Printed thin-walled structure (the text "EFL"); and (c) Printed large-inclination structure.

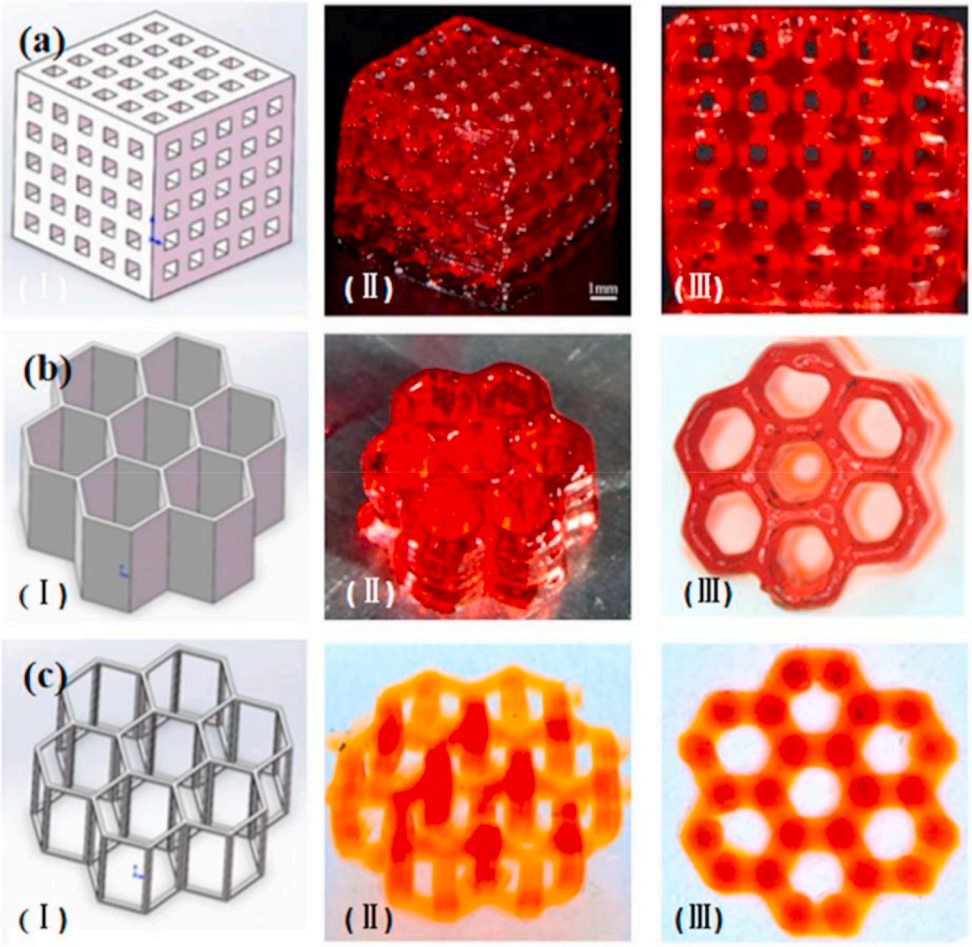

Fig. 7. Printed bionic structures. (a) Printed porous scaffold for nutrition transport; (b) Printed thin-plate liver unit structures; and (c) Printed truss liver unit structures.

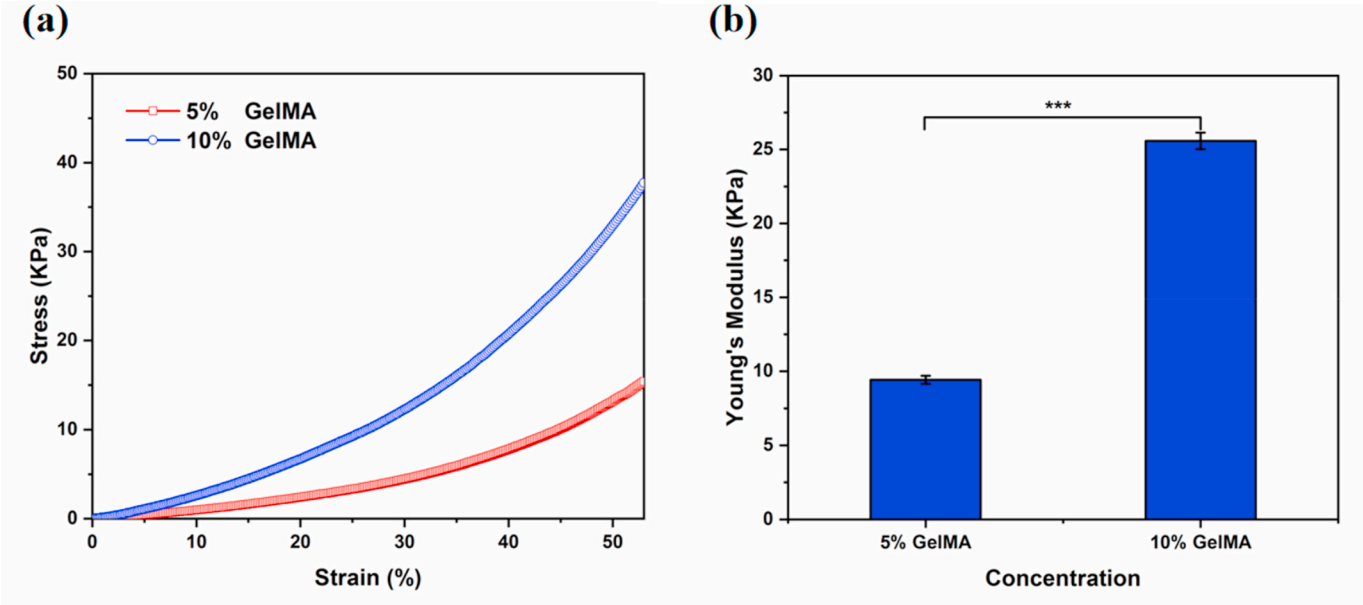

Fig. 8. Mechanical characterization of the constructs. (a) Stress/strain curves of grid structure with different GelMA concentration; (b) Young's modulus of grid structure with different GelMA concentration.

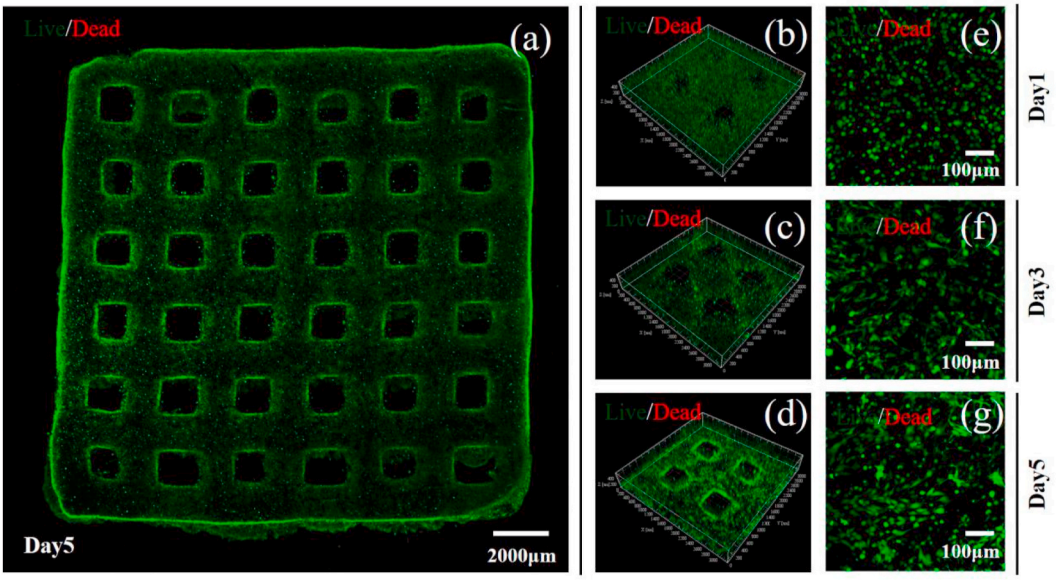

Fig. 9. Cell viability analysis. (a) Cell LIVE/DEAD staining of the mBMSC-laden GelMA scaffolds; (b–d) A 3D view of the cell LIVE/DEAD staining of GelMA scaffolds on Days 1, 3, and 5; and (e–g) Partly enlarged view of the cell Live/Dead staining of GelMA scaffolds on Days 1, 3, and 5.

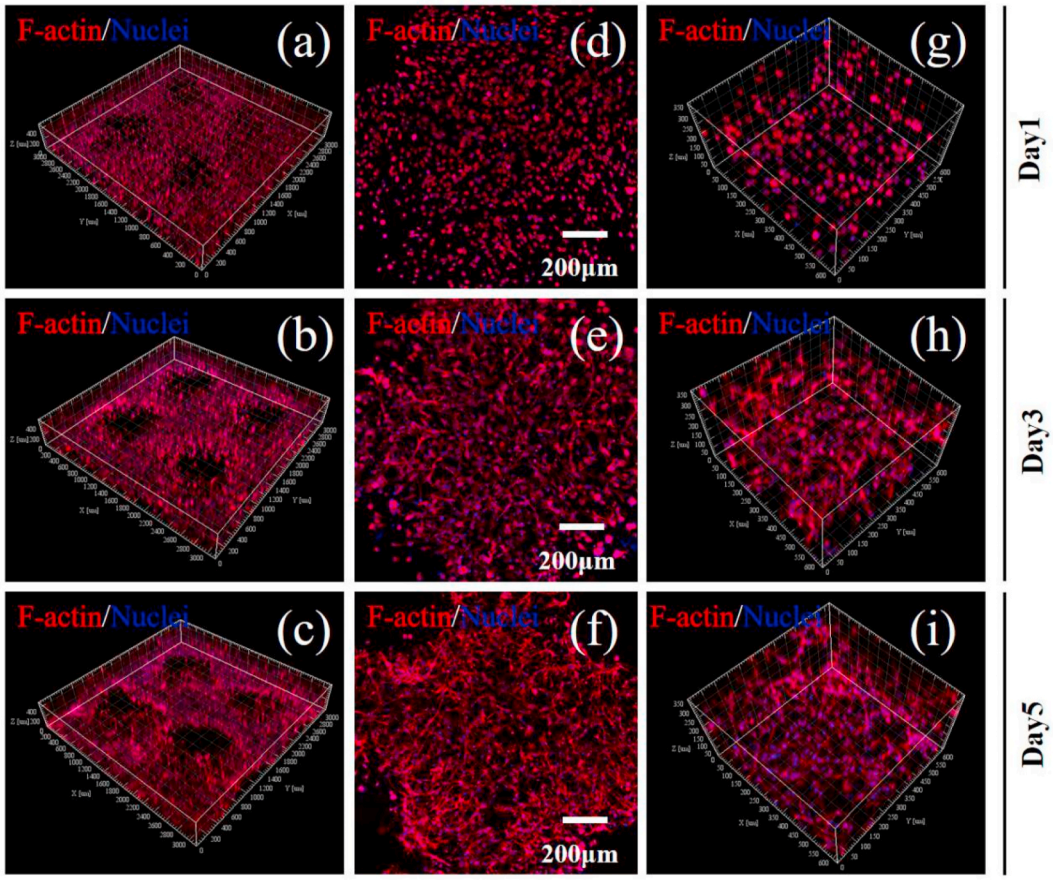

Fig. 10. Cytoskeleton staining of the mBMSC-laden GelMA scaffolds. (a–c) 3D cytoskeleton staining view of GelMA scaffolds on Days 1, 3, and 5; (d–f) Partly enlarged view of the cytoskeleton staining of GelMA scaffolds on Days 1, 3, and 5; (g–i) Partly enlarged view of the 3D cytoskeleton staining of GelMA scaffolds on Days 1, 3, and 5.

the GelMA scaffolds, and the overall geometric shape of the GelMA scaffolds is not apparent. The cells appear spherical on day 1. Also, as shown in Fig. 9(c) and (f), the cells gradually migrate to the surface of the GelMA scaffolds, and the number of cells at the edge of the scaffolds is greater than that of cells in the interior of the scaffolds, and the cells start appearing elongated on day 3. The images in Fig. 9(d) and (g)

reveal that the cells gather on the surface of the GelMA scaffolds by cell division and proliferation, and the geometry of the GelMA scaffolds can be clearly identified by LIVE/DEAD staining on day 5. The grid pores are clearly visible, the cells gradually elongate, linking to one another and initially showing the functional cell morphology. After culturing for 5 days, mBMSCs showed excellent survival on the GelMA scaffold, had stretched appearance and migrated exhibiting certain functional structures.

3.5.2. Cell morphological analysis

The images of the experiments to determine cell survival, extension, and migration of mBMSCs on the mBMSC-laden GelMA scaffolds on days 1, 3, and 5 are shown in Fig. 10. As shown in Fig. 10(a)–(c), with increasing culture time, the cells stretch and migrate in the hydrogel, clearly showing the 3D structure of the GelMA scaffolds. In Fig. 10(d)–(f), most of the cells in the interior of the GelMA scaffolds migrate to the surface, indicating that cells can migrate freely inside the GelMA scaffolds after culturing for 5 d. In Fig. 10(g)–(i), the morphology of the cells changes with the extension of culture time. In mBMSC tissue, a reticular "functional structure" of cross-connection exists between cells, indicating the extension and functionalization of cells in the hydrogel. In summary, the mBMSC-laden GelMA scaffolds printed with the SL bioprinting system enables the cells to survive, stretch, and migrate inside the scaffolds.

4. Conclusion

In this study, a lightweight SL bioprinting system was developed. This printing system enables the convenient printing of complex bionic structures while maintaining good biocompatibility. By systematically evaluating the point-by-point curing process in the 3D bioprinting method with photocrosslinkable bioinks, we explained the formation mechanism underlying the visible light-curing process of hydrogels. Additionally, we systematically analyzed the relationship between printing accuracy, printing speed, hydrogel concentration, biocompatibility, and other factors. The results demonstrated that this SL bioprinting system provides an efficient and low-cost strategy for the printing of complex structures with excellent shape fidelity using photocrosslinkable bioinks. This strategy has great potential for widespread application in drug screening, the study of pathological mechanisms of diseases, and the development of biological disease models.

CRediT authorship contribution statement

Peng Zhang: Conceptualization, Methodology, Formal analysis, Writing - original draft. **Haoxuan Wang:** Software, Data curation. **Peng Wang:** Visualization. **Yating Zheng:** Data curation, Investigation. **Linxiang Liu:** Validation, Resources. **Jun Hu:** Resources. **Yande Liu:** Funding acquisition, Supervision. **Qing Gao:** Supervision, Writing - review & editing, Funding acquisition. **Yong He:** Conceptualization, Project administration.

Declaration of competing interest

We declare that we do not have any commercial or associative interest that represents a conflict of interest in connection with the work submitted.

Acknowledgments

The authors gratefully acknowledged the financial support of National 863 Program (SS2012AA101306), "the 12th Five-Year Plan", Jiangxi Advantageous Science and Technology Innovation Team Construction Plan (20153BCB24002), Collaborative Innovation Center Project of Intelligent Management Technology and Equipment for Southern Mountain Orchards (G.J.G.Z. [2014] No.60), National Natural Science Foundation of China (2002017018, 51805474), and the China Postdoctoral Science Foundation (Grant No. 2019T120509).

Appendix ASupplementary data

Supplementary data to this article can be found online at https://doi.org/10.1016/j.bioactmat.2020.10.023.

References

[1] S. Naahidi, M. Jafari, M. Logan, Y. Wang, Y. Yuan, H. Bae, B. Dixon, P. Chen, Biocompatibility of hydrogel-based scaffolds for tissue engineering applications, Biotechnol. Adv. (2017) 530.
[2] L.-G. Griffith, G. Naughton, Tissue engineering–current challenges and expanding opportunities, Science 5557 (2002) 1009–1014.
[3] R. Langer, J. Vacanti, Tissue engineering, Mol. Ther. 1 (2000) 12–15.
[4] X. Cui, K. Breitenkamp, M.-G. Finn, Direct human cartilage repair using three-dimensional bioprinting technology, Tissue Eng. (2012) 1304–1312.
[5] A. S, K. A, A perspective on 3D bioprinting in tissue regeneration, Bio-design and manufacturing 3 (2018) 157–160.
[6] M.-M. Laronda, A.-L. Rutz, S. Xiao, K.-A. Whelan, F.-E. Duncan, E.-W. Roth, T.-K. Woodruff, R.-N. Shah, A bioprosthetic ovary created using 3D printed microporous scaffolds restores ovarian function in sterilized mice, Nat. Commun. (2017) 15261.
[7] V. Mironov, V. Kasyanov, R.-R. Markwald, Organ printing: From bioprinter to organ biofabrication line, Curr. Opin. Biotechnol. 5 (2011) 667–673.
[8] M. Hospodiuk, M. Dey, D. Sosnoski, I.-T. Ozbolat, The bioink: A comprehensive review on bioprintable materials, Biotechnol. Adv. 2 (2017) 217–239.
[9] J. Van Hoorick, L. Tytgat, A. Dobos, H. Ottevaere, S. Van Vlierberghe, (Photo-) crosslinkable gelatin derivatives for biofabrication applications, Acta Biomater. 97 (2019).
[10] M. Costantini, J. Idaszek, K. Szke, J. Jaroszewicz, W. Wiszkowski, 3D bioprinting of BM-MSCs-loaded ECM biomimetic hydrogels for in vitro neocartilage formation, Biofabrication 3 (2016) 35002.
[11] S.-H. Kim, Y.-K. Yeon, J.-M. Lee, J.-R. Chao, Y.-J. Lee, Y.-B. Seo, M.-T. Sultan, O.-J. Lee, J.-S. Lee, S.-I. Yoon, Precisely printable and biocompatible silk fibroin bioink for digital light processing 3D printing, Nat. Commun. 1 (2018) 1620.
[12] J. Van Hoorick, H. Declercq, A. De Muynck, A. Houben, L. Van Hoorebeke, R. Cornelissen, J. Van Erps, H. Thienpont, P. Dubruel, S. Van Vlierberghe, Indirect additive manufacturing as an elegant tool for the production of self-supporting low density gelatin scaffolds, J. Mater. Sci. Mater. Med. 10 (2015) 241–247.
[13] Z. Wang, R. Abdulla, B. Parker, R. Samanipour, S. Ghosh, A simple and high-resolution stereolithography-based 3D bioprinting system using visible light crosslinkable bioinks, Biofabrication 4 (2015) 45009.
[14] L.-S.-S.-M. Magalhes, F.-E.-P. Santos, C. de Maria Vaz Elias, S. Afewerki, A.-O. Lobo, Printing 3D hydrogel structures employing low-cost stereolithography technology, J. Funct. Biomater. 11 (1) (2020).
[15] H. Jian, M. Wang, S. Wang, A. Wang, S. Bai, 3D Bioprinting for Cell Culture and Tissue Fabrication, Bio-Design and Manufacturing (2018) 45–61, 001.
[16] H. Quan, T. Zhang, H. Xu, S. Luo, J. Nie, X. Zhu, Photo-curing 3D printing technique and its challenges, Bioactive Materials 1 (2020) 110–115.
[17] D. Choudhury, S. Anand, M.-W. Naing, The arrival of commercial bioprinters-Towards 3D bioprinting revolution!, International Journal of Bioprinting (2018) 23–42, 002.
[18] F. Pereira, V. Parfenov, Y. Khesuani, A. Ovsianikov, Vladimir Mironov, Vladimir, commercial 3D bioprinters, 3D Printing and Biofabrication, 2018, pp. 1–16.
[19] Reference Series in Biomedical Engineering, Springer.
[20] I-S- P Biotechnol. Adv. Vol.
[21] Y. Sun, K. Yu, J. Nie, M. Sun, Y. He, Modeling the printability of photocuring and strength adjustable hydrogel bioink during projection based 3D bioprinting, Biofabrication (2020) 1758–5090.
[22] J. Koffler, W. Zhu, X. Qu, O. Platoshyn, J.-N. Dulin, J. Brock, L. Graham, P. Lu, J. Sakamoto, M. Marsala, Biomimetic 3D-printed scaffolds for spinal cord injury repair, Nat. Med. 25 (2019) 263–269.
[23] M. Xie, Q. Gao, H. Zhao, J. Nie, Z. Fu, H. Wang, L. Chen, L. Shao, J. Fu, Z. Chen, Electro-assisted bioprinting of low-concentration GelMA microdroplets, Small 15 (2018).
[24] J.-H.-Y. Chung, S. Naficy, Z. Yue, R. Kapsa, A. Quigley, S.-E. Moulton, G.-G. Wallace, Bio-ink properties and printability for extrusion printing living cells, Biomaterials 7 (2013) 763–773.
[25] C. Colosi, S.-R. Shin, V. Manoharan, S. Massa, M. Costantini, A. Barbetta, M.-R. Dokmeci, M. Dentini, A. Khademhosseini, Microfluidic bioprinting of heterogeneous 3D tissue constructs using low viscosity bioink, Adv. Mater. 4 (2016) 677–684.
[26] S.-V. Murphy, A. Atala, 3D bioprinting of tissues and organs, Nat. Biotechnol. 8 (2014) 773–785.
[27] Effect of bioink properties on printability and cell viability for 3D bioplotting of embryonic stem cells, Biofabrication 3 (2016) 35020.
[28] W. Jia, P.-S. Gungor-Ozkerim, Y.-S. Zhang, K. Yue, A. Khademhosseini, Direct 3D Bioprinting of Perfusable Vascular Constructs Using a Blend Bioink, Biomaterials, 2016, pp. 58–68.

[29] Q. Gao, X. Niu, L. Shao, L. Zhou, Z. Lin, A. Sun, J. Fu, Z. Chen, J. Hu, Y. Liu, 3D printing of complex GelMA-based scaffolds with nanoclay, Biofabrication 11 (2019) 35006.
[30] W. Yuan, Z. Li, X. Xie, Z. Zhang, L. Bian, Bisphosphonate-based nanocomposite hydrogels for biomedical applications, Bioactive Materials 5 (2020) 819–831.
[31] T. Hu, X. Cui, M. Zhu, M. Wu, X. Fu, 3D-printable supramolecular hydrogels with shear-thinning property: fabricating strength tunable bioink via dual crosslinking, Bioactive Materials 5 (2020) 808–818.
[32] A. Ribeiro, M.-M. Blokzijl, R. Levato, C.-W. Visser, M. Castilho, W.-E. Hennink, T. Vermonden, J. Malda, Assessing bioink shape fidelity to aid material development in 3D bioprinting, Biofabrication 10 (2017).
[33] G. Gillispie, P. Prim, J. Copus, J. Fisher, A.-G. Mikos, J. J, Assessment methodologies for extrusion-based bioink printability, Biofabrication 2 (2020) 22003.
[34] L. Ouyang, C.-B. Highley, C.-B. Rodell, W. Sun, J.-A. Burdick, 3D Printing of Shear-Thinning Hyaluronic Acid Hydrogels with Secondary Cross-Linking, Acs Biomaterials ence & Engineering, 2016, pp. 6b–158b.
[35] H. Stratesteffen, M. Köpf, F. Kreimendahl, A. Blaeser, S. Jockenhoevel, A.-H. Fischer, GelMA-collagen blends enable drop-on-demand 3D printablility and promote angiogenesis, Biofabrication 4 (2017) 45002.
[36] Xuan Zhou, Haitao Cui, Margaret Nowicki, Shida Miao, Se-Jun Lee, Three-dimensional-bioprinted dopamine-based matrix for promoting neural regeneration, ACS Appl. Mater. Interfaces 10 (2018) 8993–9001.
[37] W. Zhu, H. Cui, B. Boualam, F. Masood, E. Flynn, R. Rao, Z. Zhang, L.-G. Zhang, 3D bioprinting mesenchymal stem cell-laden construct with core-shell nanospheres for cartilage tissue engineering, Nanotechnology 29 (2018) 185101.
[38] L. Herschdorfer, W.-M. Negreiros, G.-O. Gallucci, A. Hamilton, Comparison of the accuracy of implants placed with CAD-CAM surgical templates manufactured with various 3D printers: An in vitro study, J. Prosthet. Dent 3 (2020).
[39] X. Zhou, N.-J. Castro, W. Zhu, H. Cui, M. Aliabouzar, K. Sarkar, L.-G. Zhang, Improved human bone marrow mesenchymal stem cell osteogenesis in 3D bioprinted tissue scaffolds with low intensity pulsed ultrasound stimulation, For. Rep. 6 (2016) 32876.
[40] F.-P.-W. Melchels, K. Bertoldi, R. Gabbrielli, A.-H. Velders, J. Feijen, D.-W. Grijpma, Mathematically defined tissue engineering scaffold architectures prepared by stereolithography, Biomaterials 27 (2010) 6909–6916.
[41] F.-P.-W. Melchels, J. Feijen, D.-W. Grijpma, A review on stereolithography and its applications in biomedical engineering, Biomaterials 24 (2010) 6121–6130.
[42] C.-S. Carrell, C.-P. McCord, R.-M. Wydallis, C.-S. Henry, Sealing 3D-printed parts to poly(dimethylsiloxane) for simple fabrication of microfluidic devices, Anal. Chim. Acta (2020) 78–84.
[43] D.-N. Heo, S. Lee, R. Timsina, X. Qiu, N.-J. Castro, Development of 3D printable conductive hydrogel with crystallized PEDOT:PSS for neural tissue engineering. Materials Science & Engineering. C, Materials for Biological Applications, 2019, pp. 582–590.
[44] K. Arcaute, B.-K. Mann, R.-B. Wicker, Stereolithography of three-dimensional bioactive poly(ethylene glycol) constructs with encapsulated cells, Ann. Biomed. Eng. 9 (2006) 1429–1441.
[45] Zongjie Wang, Hitendra Kumar, Zhenlin Tian, Xian Jin, J.F. Holzman, Visible light photoinitiation of cell-adhesive gelatin methacryloyl hydrogels for stereolithography 3D bioprinting, ACS Appl. Mater. Interfaces 10 (2018) 26859–26869.